Waveform Inversion for Shear Velocity and Attenuation via the Spectral-Element Adjoint Method

Fan V. Wu, Dmitry Borisov[*1,2], Frederik J. Simons[1], and Paul Williamson[3]*
[1]*Princeton University,* [2]*Kansas Geological Survey,* [3]*Total EP Research and Technology*

SUMMARY

Intrinsic attenuation affects both amplitude and phase behavior of the seismic wavefield. Its three-dimensional distribution in the subsurface needs to be robustly estimated to make earth models accurate. Full Waveform Inversion (FWI) has become the technique of choice for recovering high-resolution velocity structure, but its ability to reliably recover attenuation variations remains challenging. Multistage and hierarchical approaches offer promise to control the delicate trade-off between resolving elastic and anelastic structure in inversions for the shear velocity V_S and quality factor Q_μ, in regimes with strong surface waves prone to cycle skipping. We present a procedure for their joint reconstruction via spectral-element adjoint-based full-waveform modeling. Starting from a checkerboard example, we develop a frequency and offset continuation strategy for onshore active-source acquisition. In the early stages of our algorithm, the inversion targets the refinement of the shear-wave speed model by gradually widening the frequency band and increasing the offset range. The shear quality factor is of major consideration only in the final stage of the inversion. Our procedure is robust, competitive, and practical.

INTRODUCTION

Intrinsic attenuation is important in exploration settings as well as for global earth models (Dahlen and Tromp, 1998). The joint estimation of velocity and attenuation parameters in viscoelastic media remains a challenge, owing to the trade-off between wave speeds (V_S, V_P) and quality factors (Q_μ, Q_κ) in influencing the seismic waveform (Virieux and Operto, 2009; Malinowski et al., 2011; Operto et al., 2013). As the seismic wavefield is most sensitive to *velocity* perturbations, hierarchically updating *elastic* before *anelastic* parameters in stages increases the stability of *attenuation* estimation under Full Waveform Inversion (Prieux et al., 2013). Such strategies may also benefit from, e.g., pseudo-Hessian preconditioning (Operto and Miniussi, 2018; Yang et al., 2018) or the use of specifically *amplitude*-sensitive misfit functions (Pan and Wang, 2020).

Cycle-skipping, non-linearity, and the non-convexity of the PDE-constrained FWI misfit function, compound the difficulty of Q inversions. Common solutions are multiscale: selecting low-frequency waveform-components first and gradually moving up gently guides the model updates away from local minima (Bunks et al., 1995; Fichtner, 2010; Yuan and Simons, 2014). Numerous details and parameter choices need to be settled on for practical applications. We show a checkerboard scenario where body waves dominate, and an onshore active-source experiment where surface waves lead to cycle-skipping.

Combining a two-stage strategy with a multiscale approach, deferring the joint inversion for velocity and attenuation until the second stage, is preferable, as we show numerically.

METHOD

The viscoelastic wave equation is (Dahlen and Tromp, 1998):

$$\rho(\mathbf{x})\ddot{u}_i(\mathbf{x},t) - \partial_{x_j}\int_{-\infty}^{t} C_{ijkl}(\mathbf{x},t-\tau)\dot{\varepsilon}_{kl}(\mathbf{x},\tau)\mathrm{d}\tau = f_i(\mathbf{x},t), \quad (1)$$

where $\rho(\mathbf{x})$ is the mass density at position $\mathbf{x}$, $C_{ijkl}(t)$ is the time-dependent elastic tensor (bulk and shear moduli $\kappa(t)$ and $\mu(t)$ under isotropy). With the quality factor Q the ratio between the real and the imaginary parts of the frequency-domain moduli, adopting a constant-Q absorption-band model, the dispersion relationship about reference frequency ω_0 is given by

$$C(\omega) = C(\omega_0)\left(1 + \frac{2}{\pi Q}\ln\frac{|\omega|}{\omega_0}\right). \quad (2)$$

Hence, model parameters are ρ, $\kappa(\omega_0)$, $\mu(\omega_0)$, Q_κ, and Q_μ.

The waveform-difference sensitivity kernels with respect to ρ, κ, and μ have the same form as in the elastic case (Tromp et al., 2005). Those for Q_κ and Q_μ may be calculated by introducing adjoint forces for attenuation in the frequency domain, $\tilde{f}^\dagger_{i,Q}$, which relate to the corresponding elastic adjoint forces $\tilde{f}^\dagger_i$ as

$$\tilde{f}^\dagger_{i,Q}(\mathbf{x},\omega) = \left[\frac{2}{\pi}\ln\frac{|\omega|}{\omega_0} - i\,\mathrm{sgn}(\omega)\right]\tilde{f}^\dagger_i(\mathbf{x},\omega). \quad (3)$$

Forward simulations employ the spectral-element method (Komatitsch and Tromp, 1999), which handles surface topography extremely well. For our optimization, we use the parameters ρ, V_S, V_P, Q_κ^{-1} and Q_μ^{-1}. The variation of the misfit function $\delta\chi$ and the kernels for the new parametrization relate as follows:

$$\delta\chi = \int \Big[K'_\rho\,\delta\ln\rho + K_{V_P}\,\delta\ln V_P + K_{V_S}\,\delta\ln V_S + K^Q_\kappa\,\delta Q_\kappa^{-1} + K^Q_\mu\,\delta Q_\mu^{-1}\Big]\,\mathrm{d}^3\mathbf{x}, \quad (4)$$

where K^Q_κ and K^Q_μ have the same expression as K_κ and K_μ except for replacing the adjoint forces.

Wavefield computations are done using SPECFEM2D. We use SeisFlows (Modrak et al., 2018) to make waveform-difference measurements. For optimization we use L-BFGS, a line search algorithm, well suited for large-scale optimization (Nocedal and Wright, 2006).

SYNTHETIC EXAMPLE I: CHECKERBOARD

To examine the performance of different two-stage inversion procedures for V_S and Q_μ we present a checkerboard example with 10% and 80% perturbation, respectively. The initial models are homogeneous. Fig. 1 shows the data coverage, with 25 sources and 132 receivers. Inversion parameters, misfit functions, number of iterations, frequency band, etc, need to be specified at each stage. We mainly discuss the effect of the choice of inversion parameters per stage. See Table 1.

	stage 1		stage 2	
Nr	iterations	parameters	iterations	parameters
1	20	V_S	80	V_S, Q_μ
2	20	V_S	80	Q_μ
3	50	V_S, Q_μ	50	Q_μ
4	20	V_S, Q_μ	80	V_S, Q_μ
5	20	V_S, Q_μ(drop)	80	V_S, Q_μ

Table 1: Checkerboard experiment: inversion procedures, with V_S of primary interest in stage 1, and Q_μ in stage 2. The total number of inversion steps is constant. Procedure 5 inverts for V_S and Q_μ jointly in stage 1, but discards the Q_μ model result.

Fig. 2 shows final inverted V_S and Q_μ models. We do not show results for procedure 2, unsuccessful regardless of the number of steps in stage 1. All major features of the target model appear to be resolved in regions with good data coverage. Procedure 3 fails when V_S and Q_μ are inverted jointly for 20 iterations. This implies that inverting for Q_μ alone in stage 2 places strong requirements on the accuracy of the V_S model from the prior stage. Procedure 2 failed because no accurate V_S model can be obtained by inverting for V_S alone in stage 1.

Fig. 3 shows model and data misfits over the iterations. Fig. 3a shows how V_S model misfits drop faster for the case where V_S and Q_μ are jointly inverted for. All misfits converge slower in later iterations for procedure 3, which suggests that the Q_μ model can hardly be improved further without updating V_S. We note that procedure 5 yielded the lowest Q_μ model misfit, which shows that we can safely ignore any previous inverted Q_μ model and update it with the initial model. Such strategy can be adopted when a reliable Q_μ model can not be obtained in the first stage, where it simply may act as a nuisance parameter with respect to the main model parameters.

We draw the following conclusions from the inversion results above. In the first stage, inverting for V_S by itself, or jointly with Q_μ, are possible choices, but both have limitations. Inverting for V_S alone slows down convergence of the V_S model. However, when both V_S and Q_μ are jointly inverted for, the Q_μ model of the first stage could be far from the truth. This motivated procedure 5. In the second stage, we recommend inverting for V_S and Q_μ jointly. Inverting for Q_μ alone requires a very accurate V_S model from the previous stage, and slows down convergence after the first few updates. Inverting for V_S and Q_μ jointly is the strategy of choice at that stage.

SYNTHETIC EXAMPLE II: ONSHORE

The second synthetic example is based on an onshore active-source experiment. Initial and true models are illustrated in Fig. 4. The true model has two gaussian-smoothed rectangular -30% V_S and -60% to $+300\%$ Q_μ anomalies. One is a low-velocity, high-attenuation anomaly, the other is low-velocity, low-attenuation anomaly. No relationship between V_S and Q_μ was fixed, so as to test whether the procedure works in very general settings. The experiment places 64 surface sources at an interval of 80 m. There are 270 surface receivers.

Cycle-skipping is a major challenge for onshore elastic FWI, best addressed by progressive data selection. We adopt the frequency and offset continuation strategy of Borisov et al. (2020). The procedure now consists of five stages. In each stage, V_S and Q_μ are jointly inverted for, but Q_μ is discarded at the end of every stage. From stage 1 to stage 4 we sequentially widen the frequency bands, starting from 5 Hz to 7.5, 10, 12.5, and 15 Hz, and offsets from 300 m to 700, 1000, 1200, and 1500 m. In stage 5 we jointly invert for V_S and Q_μ, within the frequency band 5–15 Hz and for offsets from 300–1500 m.

Fig. 5 shows the inverted V_S models after stages 1, 3, and 5, and Fig. 6 shows the corresponding data and model misfits. The normalized data misfit, Fig. 6a, shows a substantial reduction with each stage. From stages 2 to 4, the data misfit at the beginning of each stage increases with the widening of the frequency band. The V_S anomalies are clearly recovered after stage 1, but the V_S model continuous to improve in later stages, as shown by Fig. 6b. The inverted Q_μ models display quite different behavior. In stage 1, only one of the anomalies is reasonably recovered, whereas the update for the other part heads in the wrong direction, as seen in Fig. 5d, and in Fig. 6c. As the V_S model gradually becomes better constrained, the update to Q_μ reverses direction, and hence both Q_μ anomalies can be resolved. It is worth mentioning that continuing the Q_μ model update in the next stage from the inverted model in the previous stage does not facilitate getting out of local minima, hence our discarding the Q_μ model before every next stage.

Two alternative procedures also combine multiple stages with frequency and offset continuation. The first is a simple modification of the one just discussed, except that from stages 1 to 4, only V_S is inverted for. After two stages, the V_S model cannot further be improved, which suggests that without updating Q_μ, V_S could be trapped in local minimum. The comparison of data and model misfits in Fig. 7 clearly suggests that updating V_S and Q_μ simultaneously outperforms updating V_S alone.

To determine when to begin including Q_μ, we designed the second alternative. Stages 1–3 are identical to the original method, inverting for V_S and Q_μ, continuing on in stage 4 without discarding the Q_μ result. The misfit functions are shown in Fig. 8. The original procedure outperforms this second alternative. The same conclusion holds whether we treat stages 2 or 3 as the final stage for Q_μ inversion. We conclude that a suitable stage to begin the Q_μ inversion without further resetting is when the V_S model has considered all the available data.

CONCLUSION

Shear velocity and quality factor perturbations can be reconstructed using a multistage frequency and offset continuation inversion strategy. Carrying out separate inversions for V_S and Q_μ converges slowly, and possibly far from the truth, due to cycle-skipping and parameter trade-offs. Inverting jointly for V_S and Q_μ in each stage, best results are obtained when the Q_μ model is reset at the beginning of each new stage, until V_S has been fully updated with all available data. In the final stage V_S and Q_μ can be jointly inverted for.

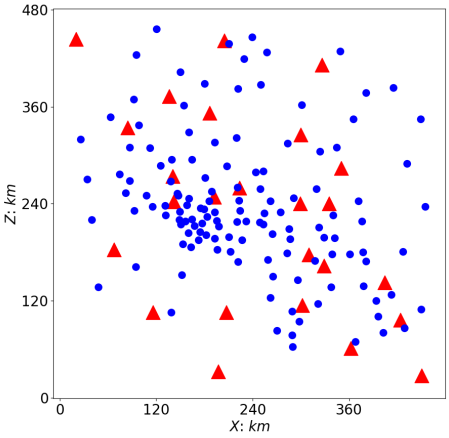

Figure 1: Location of sources (filled blue circles) and receivers (red triangles) for the checkerboard experiment of Figures 2 and 3, overlying a featureless initial model.

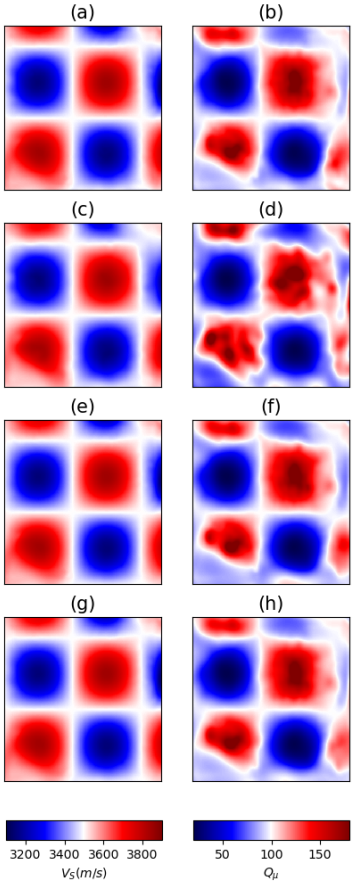

Figure 2: Checkerboard test inversion results according to the procedures 1, 3, 4, and 5 listed in Table 1. Left column: inverted shear wave speed models. Right column: inverted shear quality factor model. From top to bottom, the rows show the inverted models obtained using procedures 1, 3, 4, and 5.

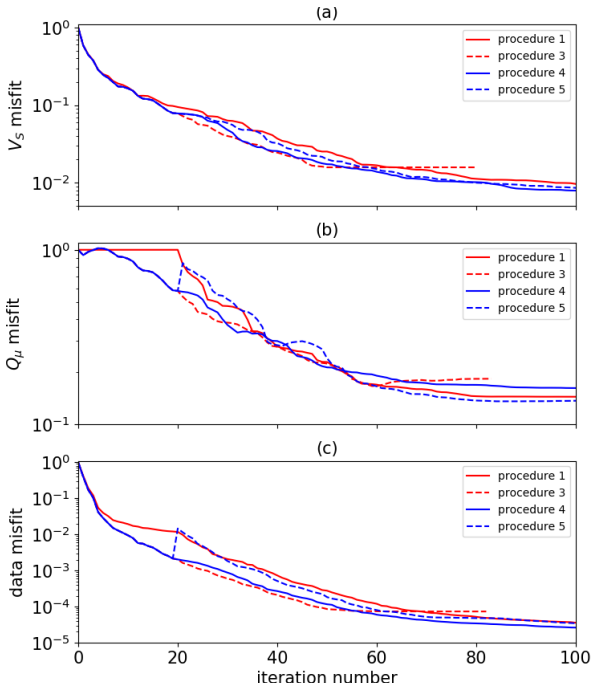

Figure 3: Evolution of model and data misfit for the checkerboard experiment with different procedures, (a) for V_S model, (b) for Q_μ model, and (c) for data misfit. Red solid line for procedure 1, red dashed line for procedure 3, blue solid line for procedure 4, and blue dashed line for procedure 5.

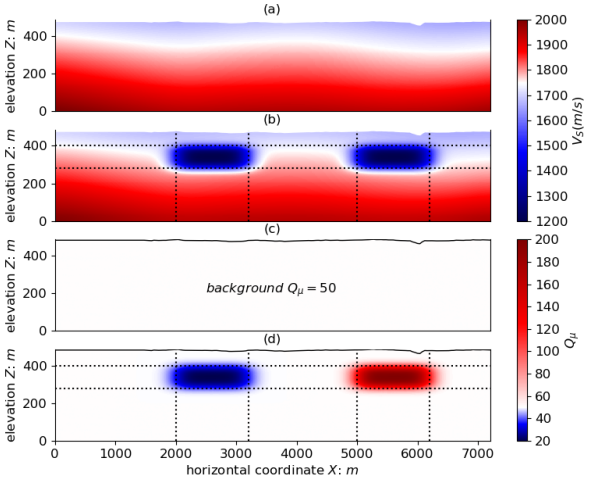

Figure 4: Initial and true models for the onshore experiment. Wave speed (a) initial V_S and (b) true V_S model. Quality factor (c) initial Q_μ and (d) true Q_μ model. Background $Q_\mu = 50$.

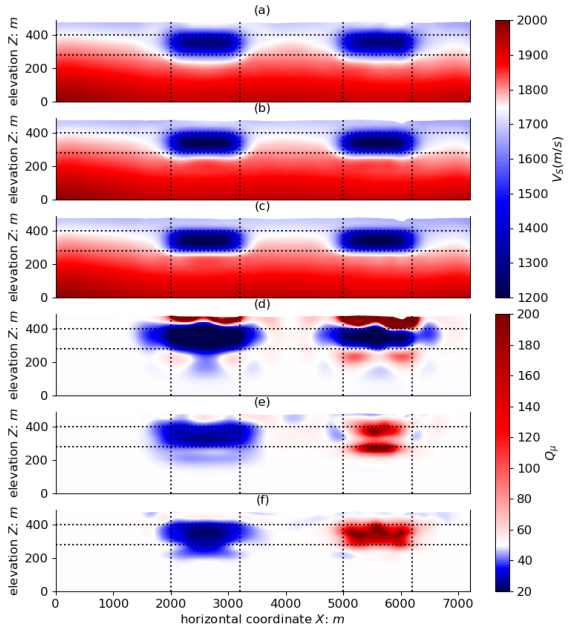

Figure 5: Inverted shear wave speed and quality factor models at different stages, for the onshore inversion experiment. Inverted velocity models (a) V_S after stage 1, (b) V_S after stage 3, and (c) V_S after stage 5. Inverted quality factor models (d) Q_μ after stage 1, (e) Q_μ after stage 3, and (f) Q_μ after stage 5.

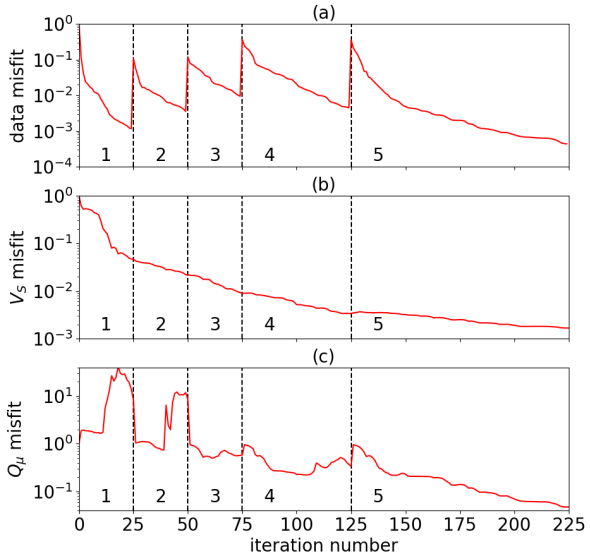

Figure 6: Evolution of data and model misfit in the onshore experiment during the five stages as noted. (a) Evolution of the data misfit. (b) Evolution of the V_S model misfit and (c) evolution of the Q_μ model misfit.

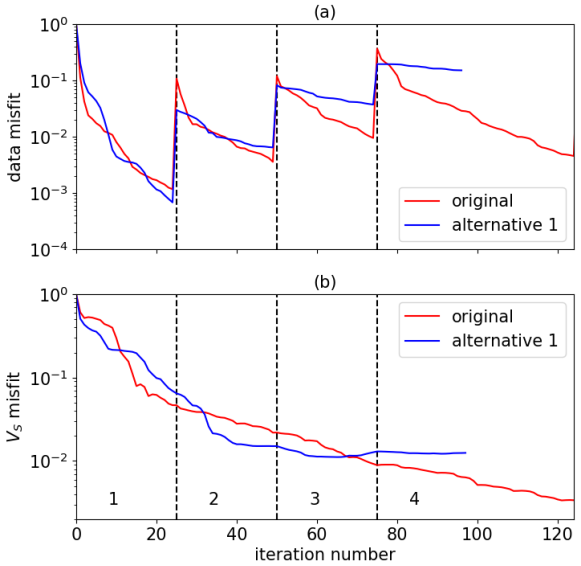

Figure 7: Comparison of the data and model misfit functions between the original procedure (red) and alternative procedure 1, which does not update Q_μ (blue). (a) Evolution of the data misfits and (b) evolution of the V_S model misfits.

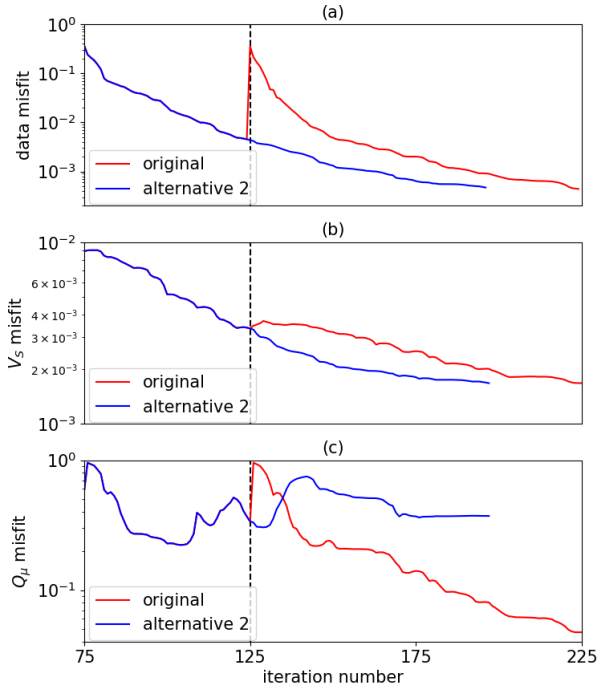

Figure 8: Comparison of the data and model misfit functions between the original procedure and alternative procedure 2. (a) Comparison between data misfits, (b) comparison between V_S model misfit and (c) comparison between Q_μ model misfits.

REFERENCES

Borisov, D., F. Gao, P. Williamson, and J. Tromp, 2020, Application of 2D full-waveform inversion on exploration land data: Geophysics, **85**, R75–R86, doi: https://doi.org/10.1190/geo2019-0082.1.

Bunks, C., F. M. Saleck, S. Zaleski, and G. Chavent, 1995, Multiscale seismic waveform inversion: Geophysics, **60**, 1457–1473, doi: https://doi.org/10.1190/1.1443880.

Dahlen, F. A., and J. Tromp, 1998, Theoretical global seismology: Princeton University Press.

Fichtner, A., 2010, Full seismic waveform modelling and inversion: Springer.

Komatitsch, D., and J. Tromp, 1999, Introduction to the spectral element method for three-dimensional seismic wave propagation: Geophysical Journal International, **139**, 806–822, doi: https://doi.org/10.1046/j.1365-246x.1999.00967.x.

Malinowski, M., S. Operto, and A. Ribodetti, 2011, High-resolution seismic attenuation imaging from wide-aperture onshore data by visco-acoustic frequency-domain full-waveform inversion: Geophysical Journal International, **186**, 1179–1204, doi: https://doi.org/10.1111/j.1365-246X.2011.05098.x.

Modrak, R. T., D. Borisov, M. Lefebvre, and J. Tromp, 2018, SeisFlows — Flexible waveform inversion software: Computers and Geosciences, **115**, 88–95, doi: https://doi.org/10.1016/j.cageo.2018.02.004.

Nocedal, J., and S. J. Wright, 2006, Numerical optimization, 2nd ed.: Springer.

Operto, S., Y. Gholami, V. Prieux, A. Ribodetti, R. Brossier, L. Metivier, and J. Virieux, 2013, A guided tour of multiparameter full-waveform inversion with multicomponent data: From theory to practice: The Leading Edge, **32**, 1040–1054, doi: https://doi.org/10.1190/tle32091040.1.

Operto, S., and A. Miniussi, 2018, On the role of density and attenuation in three-dimensional multiparameter viscoacoustic VTI frequency-domain FWI: An OBC case study from the North Sea: Geophysical Journal International, **213**, 2037–2059, doi: https://doi.org/10.1093/gji/ggy103.

Pan, W., and Y. Wang, 2020, On the influence of different misfit functions for attenuation estimation in viscoelastic full-waveform inversion: Synthetic study: Geophysical Journal International, **221**, 1292–1319, doi: https://doi.org/10.1093/gji/ggaa089.

Prieux, V., R. Brossier, S. Operto, and J. Virieux, 2013, Multiparameter full waveform inversion of multicomponent ocean-bottom-cable data from the Valhall field — Part 1: Imaging compressional wave speed, density and attenuation: Geophysical Journal International, **194**, 1640–1664, doi: https://doi.org/10.1093/gji/ggt177.

Tromp, J., C. Tape, and Q. Liu, 2005, Seismic tomography, adjoint methods, time reversal and banana-doughnut kernels: Geophysical Journal International, **160**, 195–216, doi: https://doi.org/10.1111/j.1365-246X.2004.02453.x.

Virieux, J., and S. Operto, 2009, An overview of full-waveform inversion in exploration geophysics: Geophysics, **74**, no. 6, WCC1–WCC26, doi: https://doi.org/10.1190/1.3238367.

Yang, P., R. Brossier, L. Metivier, J. Virieux, and W. Zhou, 2018, A time-domain preconditioned truncated Newton approach to visco-acoustic multiparameter full waveform inversion: SIAM Journal on Scientific Computing, **40**, B1101–B1130, doi: https://doi.org/10.1137/17M1126126.

Yuan, Y. O., and F. J. Simons, 2014, Multiscale adjoint waveform-difference tomography using wavelets: Geophysics, **79**, no. 3, WA79–WA95.